

pubs.acs.org/JPCC Article

# High-Temperature Water Adsorption Isotherms and Ambient Temperature Water Diffusion Rates on Water Harvesting Metal—Organic Frameworks

Jon Hastings, Thomas Lassitter, Zhiling Zheng, Saumil Chheda, J. Ilja Siepmann, Laura Gagliardi, Omar M. Yaghi, and T. Grant Glover\*



Cite This: J. Phys. Chem. C 2024, 128, 11328-11339



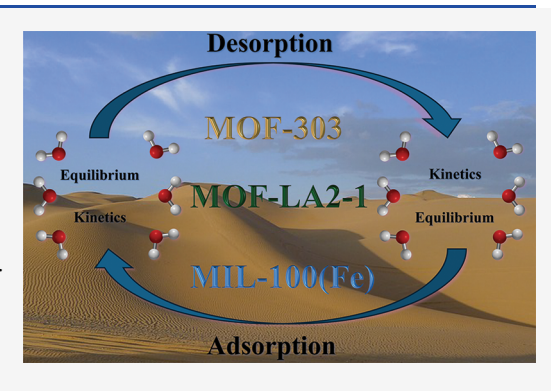
**ACCESS** I

III Metrics & More

Article Recommendations

Supporting Information

ABSTRACT: Water adsorption isotherms from 25 to 125 °C were measured for three metal—organic frameworks (MOFs), MOF-303, MOF-LA2-1, and MIL-100(Fe), which are frequently studied for water harvesting applications. The results show how the step in the water adsorption isotherm varies as a function of temperature and detail the combination of pressure and temperature necessary to remove adsorbed water. Furthermore, isobaric—isothermal Gibbs ensemble Monte Carlo simulations performed for MOF-303 shed light on the change in occupation numbers of the different known water adsorption sites with increasing temperature. Additionally, the diffusion rates of water through these materials were measured using concentration swing frequency response, and micropore diffusion was identified as the controlling mechanism. The Darken relation was used to show the dependence of the diffusion rate on the concentration and the impact of the adsorption isotherm



slope. The adsorption of water on MOF-LA2-1 is faster than that on MIL-100(Fe). These data show that MOF-LA2-1 with its highwater adsorption capacity, quick adsorption rate, and favorable desorption energetics is a leading candidate for atmospheric water harvesting.

# 1. INTRODUCTION

While the majority of the surface of our planet is covered by liquid water, only a small fraction of the water available is freshwater and also safe for human consumption. The demand for freshwater will continue to increase as a result of population growth and climate change impacts. Capturing water from the atmosphere is one approach to addressing water scarcity, and particularly, adsorption-based processes have attracted attention for this purpose. Metalorganic frameworks (MOFs), a class of porous materials made of metal ions or clusters connected together by organic ligands that create a porous framework, are appealing to complete the separation of water from other compounds in air because of their tunable pore surface chemistry, high surface area, and diversity of pore topology.

While there are numerous MOF materials, MOF-303<sup>29</sup> (Al(OH)(1-H-pyrazole-3,5-dicarboxylate), MOF-LA2-1<sup>35</sup> (Al-(OH)((E)-5-(2-carboxylatovinyl)-1H-pyrazole-3-carboxylate), and MIL-100(Fe)<sup>36</sup> (Fe<sup>III</sup><sub>3</sub>O(H<sub>2</sub>O)2F·{C<sub>6</sub>H<sub>3</sub>(CO<sub>2</sub>)<sub>3</sub>}<sub>2</sub>·nH<sub>2</sub>O) are appealing as water harvesting adsorbents because they have high water adsorption capacities at desirable relative humidities (i.e., 10–25%) near ambient temperatures compared to other compounds<sup>15,37,38</sup> and have little adsorption hysteresis. In addition to favorable adsorption isotherms, MOF-303 and MIL

materials have been produced at an industrial scale indicating that commercial deployment of these materials is feasible.<sup>39</sup>

In an adsorption based water harvesting device, the adsorbent can be heated to recover the captured water via desorption, but currently, very little thermodynamic information is available that details the water adsorption capacity of MOF materials at desorption temperatures. Moreover, the water loading at desorption/regeneration conditions is key to selecting conditions that are suitable to recover the water that has been collected but not overly aggressive such that energy is wasted heating the adsorbent. Likewise, while information about MOF-303 mass transfer rates has been reported, mass transfer rates for MOF-LA2-1 and MIL-100(Fe) have not been detailed. The combination of thermodynamics and mass transfer sets the foundation for the efficiency of any water harvesting device, and the absence of this fundamental data prevents detailed system design and process modeling.<sup>40</sup>

Received: March 15, 2024 Revised: June 11, 2024 Accepted: June 11, 2024 Published: June 28, 2024





Therefore, the purpose of this paper is to collect and detail water adsorption isotherms at temperatures above ambient on MOF-303, MOF-LA2-1, and MIL-100(Fe) and to detail the diffusion mechanism and rates of water adsorption in these materials. The data are not only relevant to process modeling for water harvesting systems but also provide insight into how reticular materials provide precise control over these parameters.

#### 2. EXPERIMENTAL SECTION

**2.1.** Metal–Organic Framework (MOF) Synthesis. MOF-303 was produced as detailed previously. <sup>41</sup> Briefly, 3,5-pyrazoledicarboxylic acid, monohydrate (H<sub>2</sub>PZDC·H<sub>2</sub>O) was dissolved in LiOH solution with H<sub>2</sub>O and heated for 30 min at 120 °C. Afterward, AlCl<sub>3</sub>·6H<sub>2</sub>O was added to the solution, and the new solution was held isothermally at 100 °C for 15 h. Then, the precipitate was collected by filtration and washed with water, before subsequently being washed with methanol for 24 h and air-dried for 3 days.

MOF-LA2-1 was produced as detailed previously. <sup>35</sup> Briefly, the linker (E)-5-(2-carboxyvinyl)-1H-pyrazole-3-carboxylic acid  $(H_2PZVDC)$  was dissolved in N,N-dimethylformamide (DMF). An aqueous solution of  $AlCl_3$ - $6H_2O$  was added dropwise, and the new solution was held isothermally for 24 h at 120 °C. After the solution was cooled to room temperature, the precipitate was collected by centrifugation and washed with  $H_2O$  and methanol before being activated under dynamic vacuum for 12 h at room temperature, followed by gradual heating to 120 °C for 6.5 h.

MIL-100(Fe) was purchased from novoMOF, and additional samples of MOF-303 were also purchased from Framergy and novoMOF.

**2.2. Breakthrough High-Temperature Water Adsorption Isotherms.** A breakthrough system was constructed similar to Lassitter et al. 40 shown in Figure S1 where a glass tube of 1.5" inside diameter was loaded with 3.11 g of sample and placed inside a chamber able to maintain temperatures ±0.1 °C to ensure thermal stability. A total flow of 200 mL min<sup>-1</sup> of helium was delivered through two mass flow controllers. The RH data acquisition was completed using LabVIEW, similar to previously reported breakthrough experiments, 42-47 and the data were used to calculate the adsorption capacity as detailed in the Supporting Information (SI). 48 The adsorption capacity calculated from breakthrough data was compared with isotherm data collected via the volumetric adsorption apparatus to validate the accuracy of the volumetric high-temperature water adsorption apparatus.

**2.3. Volumetric High-Temperature Water Adsorption Isotherms.** A volumetric adsorption apparatus was constructed similar to an apparatus constructed by Glover et al. shown in Figure S2. <sup>49</sup> The apparatus was placed inside of an environmental chamber able to maintain temperatures ±0.1 °C to ensure thermal stability. High-performance liquid chromatography (HPLC) grade liquid water, sourced from Sigma-Aldrich SHBP9108, was used as the adsorbate. The pressure was recorded using National Institute of Standards and Technology (NIST) traceable, heated capacitance-manometers from MKS Instruments, Inc. accurate to 0.01% of full scale and 0.5% of the indicated value. The accuracy values of the transducer can be used to calculate instrument readout error bars for each data point, but the bars are small enough that they are not readily observable on the isotherm plot. The leak

rate of the apparatus was measured to be  $1 \times 10^{-4}$  Torr over 2.4 h.

The volumetric measurements are based on a mass balance that requires precise measurements of the apparatus volume, and the procedure required to calculate the volumes is detailed in the SI. With the system volumes known, a sample of approximately 200–300 mg of adsorbent was inserted into the adsorbent bed. Pressure readings before and after exposure to the adsorbent were recorded using LabView. Samples were allowed to equilibrate until no change in pressure was observed for 20 min to ensure equilibrium had been reached. Additional details are given in the SI. Because the apparatus was newly constructed, the device was validated to breakthrough data, volumetric adsorption data collected on a commercial porosimeter, and to molecular simulations.

The isosteric heat of water adsorption was calculated, using a temperature range from 45 to 115  $^{\circ}$ C in 10-degree increments, by the Clausius—Clapeyron equation as detailed in the SI.  $^{50,51}$ 

**2.4. Single-Component Adsorption Isotherms.** Prior to collecting elevated temperature adsorption data, single-component adsorption data were collected using a Micromeritics 3 Flex and Micromeritics ASAP 2020 at 25 °C as shown in the SI.

2.5. Gibbs Ensemble Monte Carlo Simulations. Forcefield-based isobaric-isothermal Gibbs ensemble Monte Carlo (NpT-GEMC) simulations 52,53 were performed in the Monte Carlo for Complex Chemical Systems-MN software (MCCCS-MN)<sup>54</sup> to compute the vapor-phase unary adsorption isotherm of water in MOF-303 at 45 and 85 °C. The simulation setup and force field for MOF-303 previously used by Chheda et al.<sup>55</sup> (details of the force field are provided in the SI) were used in these simulations. Briefly, a  $3 \times 2 \times 3$  rigid supercell of the MOF structure previously optimized using periodic density functional theory (Perdew-Burke-Ernzerhof exchange-correlation density functional along with Grimme's D3 dispersion corrections with Becke-Johnson damping<sup>56</sup> and a plane-wave basis set with an energy cutoff of 520 eV) in the Vienna Ab Initio Simulation Package (VASP; version 6.2)<sup>57</sup> in the presence of water molecules adsorbed in the primary adsorption site and constrained to the cell parameters obtained using single crystal X-ray diffraction, denoted as the E4D4 structure, was used as the adsorbent phase at all temperatures.<sup>55</sup> This adsorbent box was held in thermodynamic contact with a second fluctuating-volume simulation box for the water reservoir pre-equilibrated to the target conditions. Rigid-body translational and rotational Monte Carlo moves were performed on randomly selected water molecules. Isotropic volume moves were performed on the water reservoir box to hold it at the target pressure. Swap moves were performed on the water molecules to exchange them between the reservoir and the adsorbent phase. The translational, rotational, volume, and swap analyses were randomly performed in a ratio of 0.30:0.30:0.01:0.39.

The TIP4P model was used to describe the intermolecular interactions of water molecules since it has been previously found to give a better agreement of the water adsorption isotherm in MOF-303 compared to the experimental data both when the isotherms are expressed in terms of either the absolute pressure or the relative humidity. The TIP4P was chosen over other models such as the TIP4P/2005 model which outperforms the TIP4P model when placing weight on the prediction of crystalline phases of water. However, the TIP4P/2005 water model underpredicts the vapor pressure of

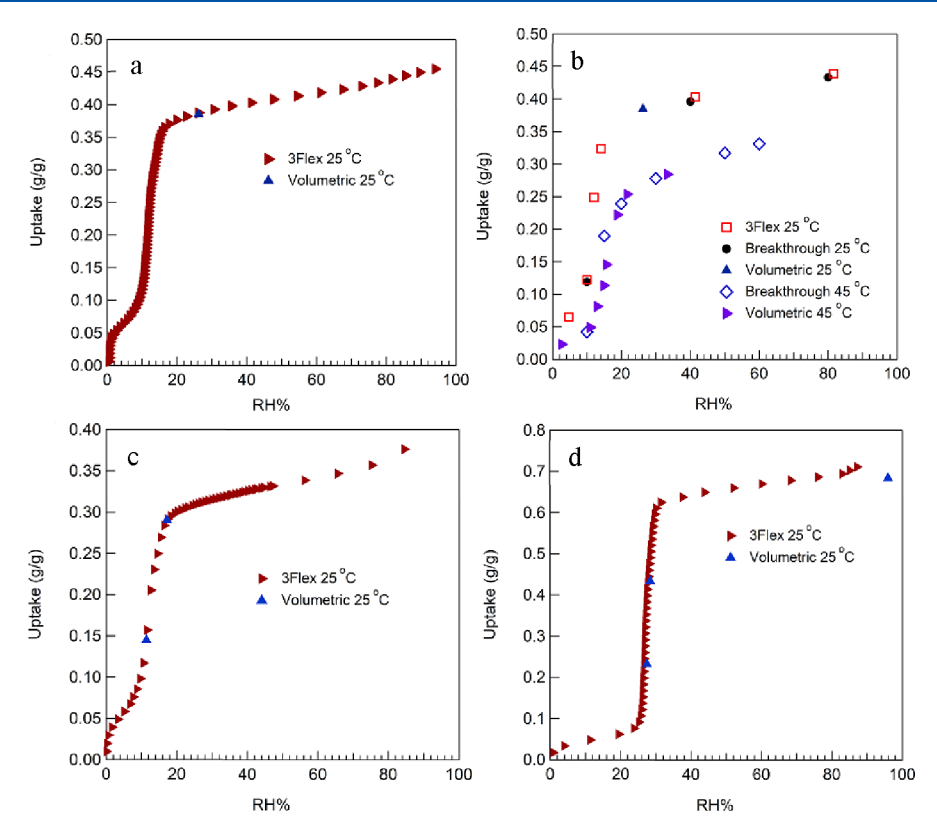


**Figure 1.** (a) 25 °C adsorption isotherms collected on the volumetric apparatus compared to commercial porosimeter for novoMOF MOF-303, (b) MOF-303 25 and 45 °C isotherms, (c) 25 °C adsorption isotherms collected on the volumetric apparatus compared to commercial porosimeter for Framergy MOF-303, (d) 25 °C adsorption isotherms collected on the volumetric apparatus compared to commercial porosimeter for MOF-LA2-1.

water, which implies that the TIP4P/2005 model would overpredict the strength of the water-water interactions. For the computation of the vapor-liquid coexistence curve of neat water, this problem can be addressed by adding a polarization correction (e.g., an isolated water molecule can lower its energy by changing from the polarized charge distribution appropriate for condensed phases mimicked by TIP4P/2005 to a nonpolarized state). Although the TIP4P/2005 model performs well for neat water, it does not perform well for mixtures. Xue et al. have compared the performance of simple nonpolarizable models for water/alkane mixtures (where the alkanes are described by the TraPPE force field) and found that the TIP4P model performs significantly better for these mixtures.<sup>61</sup> Unfortunately, there is no simple way to account for changes in polarization for water molecules in the diverse environments offered by MOF-303 and therefore, TIP4P was used.

The MOF structure was held rigid through the simulation, and thus, the intraframework interactions of the MOF were excluded. The pairwise Lennard–Jones and Coulomb interactions were truncated by using a spherical cutoff radius of 14 Å. Beyond this cutoff radius, analytical tail corrections were included for the Lennard–Jones interactions. The cutoff radius was set to 35% of the box length for large vapor simulation boxes. The Ewald summation method was used for the electrostatic interactions with the Ewald sum convergence parameter set to  $3.2/r_{\rm cut}$ . The water adsorption simulations were performed using N=1000 water molecules and at  $p/p^{\rm sat}=0.05-0.95$ , where  $p^{\rm sat}$  is the saturated vapor pressure of the TIP4P<sup>58</sup> water model at the respective temperature ( $p^{\rm sat}=4.54\pm0.12$  kPa at 25 °C, 13.747  $\pm$  0.043 kPa at 45 °C, and 82.06

 $\pm$  0.22 kPa at 85 °C). The simulations were equilibrated for at least 150000 MCC (Monte Carlo cycles, where 1 MCC consists of *N* Monte Carlo moves) followed by another 80000 MCC for the production period. Additional details are available in the SI.

**2.6. Kinetic Data.** A concentration swing frequency (CSFR) system, similar to the one used by Glover et al., was used to complete the CSFR measurements. 40,62 Briefly, helium was passed through a water saturator cell that was located in a temperature-controlled water bath, allowing for gas phase water concentrations to be controlled by setting the water bath temperature. After regeneration, the bed was exposed to a constant feed of water in helium at the selected humidity overnight to equilibrate the bed at the selected water loading. A range of concentration swing frequencies were then examined to collect the diffusion data. Additional details are in the SI.

Transport diffusivities depend on the adsorbed phase loading, and the influence of the adsorption isotherm slope on the measured kinetic rate can be calculated by following the approach outlined by Ruthven (eqs 1–6).<sup>63</sup> In this approach, eq 1 describes the transport diffusion where  $D_t$  is the transport diffusivity that is the proportionality constant relating macroscopic flux J to a spatial concentration gradient  $\nabla c$  in Fick's law.

Equation 1 can be written in terms of the gradient in the chemical potential to produce the Maxwell–Stefan form of the flux eq (eq 2) where B is the molecular mobility, c is the total concentration in the pore, and  $\frac{\partial \mu}{\partial x}$  is the gradient in chemical potential, and substitution (eqs 3–6) leads to an expression

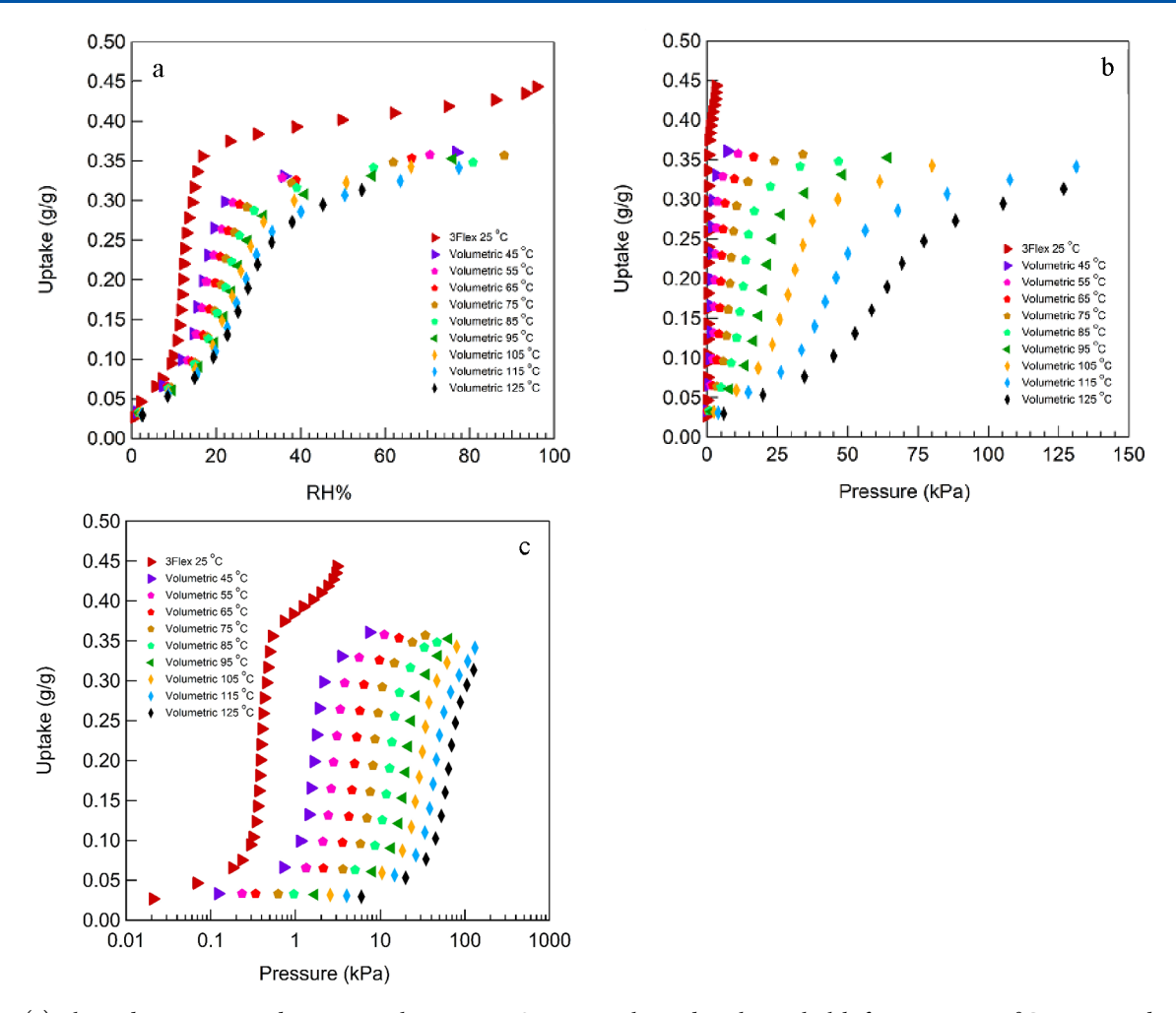


Figure 2. (a) Elevated temperature adsorption isotherms on MOF-303 synthesized in the Yaghi lab from 25 to 125 °C represented in relative humidity, (b) kPa, and (c) in semilog.

where BRT is referred to as  $D_0$ , the corrected diffusivity. <sup>58,59</sup> This term

$$J = -D_t(c)\nabla c \tag{1}$$

$$J = -Bc \frac{\partial \mu}{\partial x} \tag{2}$$

$$\mu = \mu_o + RT \ln p \tag{3}$$

$$\frac{\partial \mu}{\partial x} = RT \frac{d \ln p}{dc} \frac{\partial c}{\partial x} \tag{4}$$

$$J = -BRT \frac{d \ln p}{d \ln c} \frac{\partial c}{\partial x}$$
 (5)

$$D_{t} = BRT \frac{d \ln p}{d \ln c} \quad D_{0}\Gamma \tag{6}$$

accounts for the molecular mobility effects. The  $\frac{d \ln p}{d \ln c}$  term is referred to as the thermodynamic correction factor, and accounts for the equilibrium effects on the measured diffusivity and can also be written a  $\Gamma$ . Therefore, for a system of interest with an experimentally measured isotherm, it is possible to calculate the thermodynamic correction factor and the value of corrected diffusivity,  $D_0$ , can be determined using an experimental value of the diffusivity obtained at a particular

pressure. 63,66-69 It was assumed that the corrected diffusivity was independent of the loading. The correction factor was calculated from the isotherm data at 25 °C by utilizing a linear interpolation of the isotherm slope. While the Darken relation is an approximation, it provides an understanding of the diffusion behavior across sorbate concentrations. 63,70

# 3. RESULTS AND DISCUSSION

**3.1. Validation of Adsorption Apparatus.** Validation of the custom-built volumetric adsorption apparatus was completed by comparing water adsorption data collected on the custom-built volumetric high-temperature water adsorption apparatus to data collected on a commercially available Micromeritics 3 Flex porosimeter. Data for validation were collected on MOF-303 from different sources (Yaghi lab, novoMOF, Framenergy) and on MOF-LA2 to ensure reproducibility could be achieved regardless of sample. Additionally, validation of the volumetric apparatus was completed at different temperatures by comparing water adsorption isotherms collected volumetrically to data collected using a breakthrough device (Figure 1).

Figure 1a shows excellent agreement for water adsorption data onto MOF-303 synthesized by novoMOF that were collected on the custom-built volumetric system and on a Micromeritics 3 Flex porosimeter. Water adsorption data for MOF-303, produced by the Yaghi lab, and collected on a 3Flex

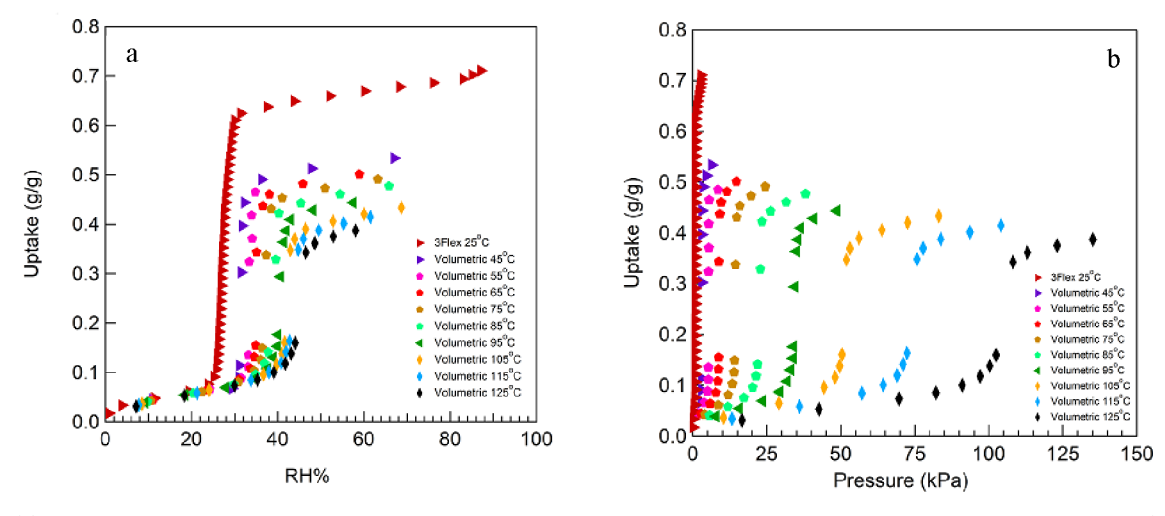


Figure 3. (a) Elevated temperature adsorption isotherms on MOF-LA2-1 from 25 to 125 °C represented in relative humidity and (b) kPa.

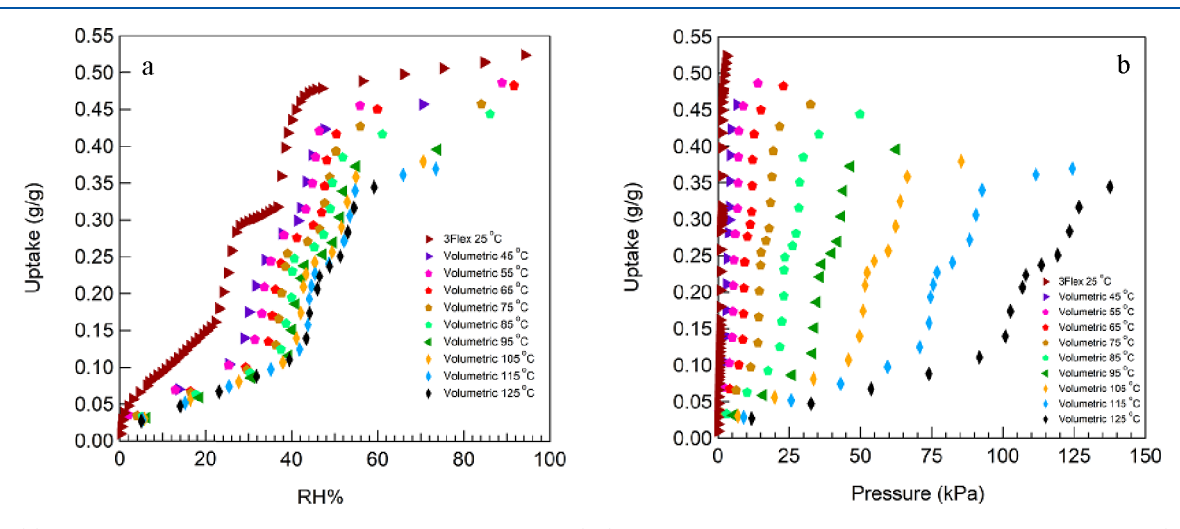


Figure 4. (a) Elevated temperature adsorption isotherms on MIL-100(Fe) from 25 to 125 °C represented in relative humidity and (b) kPa.

device, the volumetric system, and a breakthrough device are compared in Figure 1b. 40 Again, agreement across the instruments is satisfactory at 25 and 45 °C. In Figure 1c, the volumetric and 3Flex device yield consistent results for MOF-303 prepared by Framergy but with somewhat lower adsorption capacity than found for the novoMOF and Yaghilab samples. Lastly, the volumetric apparatus and the 3Flex yield excellent agreement when measuring water adsorption isotherms on MOF-LA2-1. The isotherm shape shown in Figure 1 is expected for these types of water harvesting materials as discussed elsewhere. 40,47 The results show that the volumetric apparatus built for this work is capable of measuring accurate water adsorption isotherms at and above room temperature.

**3.2.** High Temperature Pure Water Isotherms. Isotherms for pure water vapor at 25 and 45–125 °C in 10 °C increments were collected on MOF-303 (Figure 2). These isotherms show a significant decrease in the adsorption capacity from 25 to 45 °C along with a shift in the step of the isotherm toward 15% RH. The novoMOF MOF-303 25 and 45 °C isotherms (see Figures S16–S18 in SI) showed even greater reduction in adsorption capacity, but the trend was consistent with the data shown in Figure 2. The Framergy MOF-303 adsorption isotherms (see SI) showed a more modest decrease in capacity from 25 to 45 °C, but the total

capacity of the Framergy MOF-303 at 25  $^{\circ}$ C was slightly lower than that of the other sources of MOF-303.

The large decrease in loading of water upon increasing the temperature to only 45 °C (Figure 2c) makes MOF-303 an appealing candidate as a water harvesting material. Additionally, the isotherm data in Figure 2 show the precise conditions upon which the MOF can be regenerated through a combination of temperature and vacuum. For example, the data show that regeneration can be readily accomplished at 125 °C and 20 kPa or a similar loading can be obtained using 45 °C and 0.5 kPa. This type of data provides clear insight into the amount of water that remains on the adsorbent during regeneration and provides the foundation for system-level energy consumption vs water production optimization that may be required during water harvester design.

As reported previously, a linker extension strategy was used for generating MOF-LA2-1, which exhibits an approximately 50% increase in water capacity and a shift in step position toward higher RH values at 25 °C compared to MOF-303. To understand the impact on uptake at higher temperatures, water adsorption isotherms were collected up to 125 °C as shown in Figure 3. Similar trends for MOF-LA2-1 were observed as compared to those of MOF-303 where the step in the isotherm shifts toward higher relative humidity with higher temperatures, and a significant decrease in capacity is observed at 45

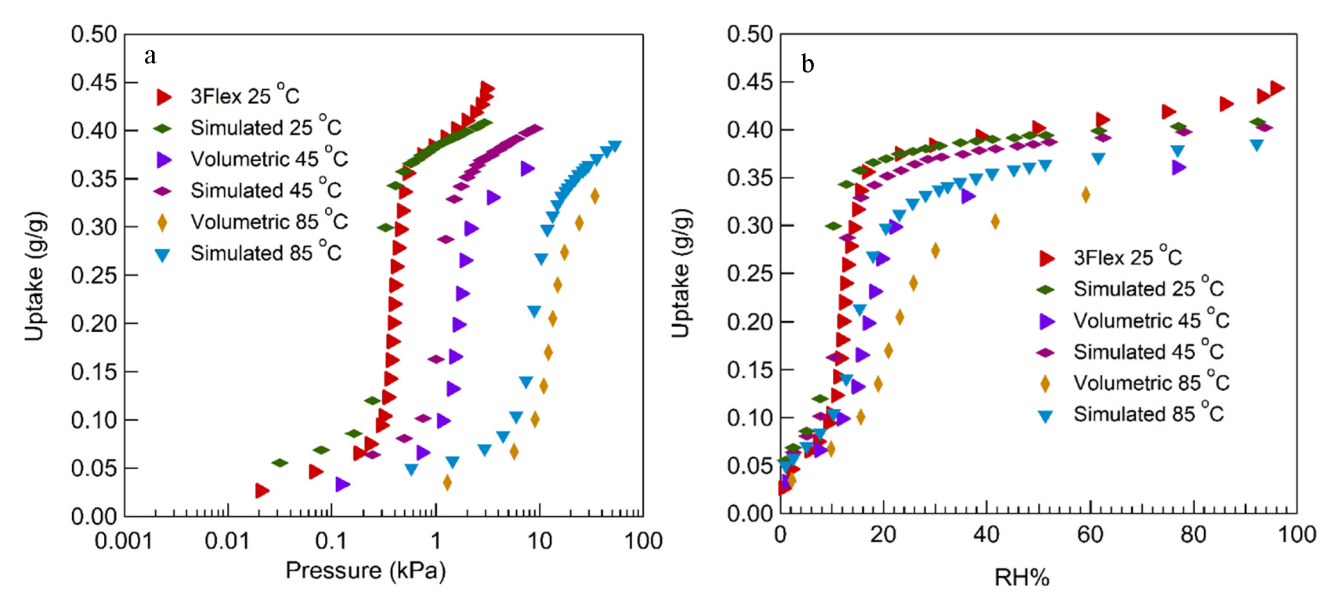


Figure 5. Comparison of synthesized MOF-303 water isotherms and water isotherms collected using GEMC simulations. The same data are shown in (a) and (b).

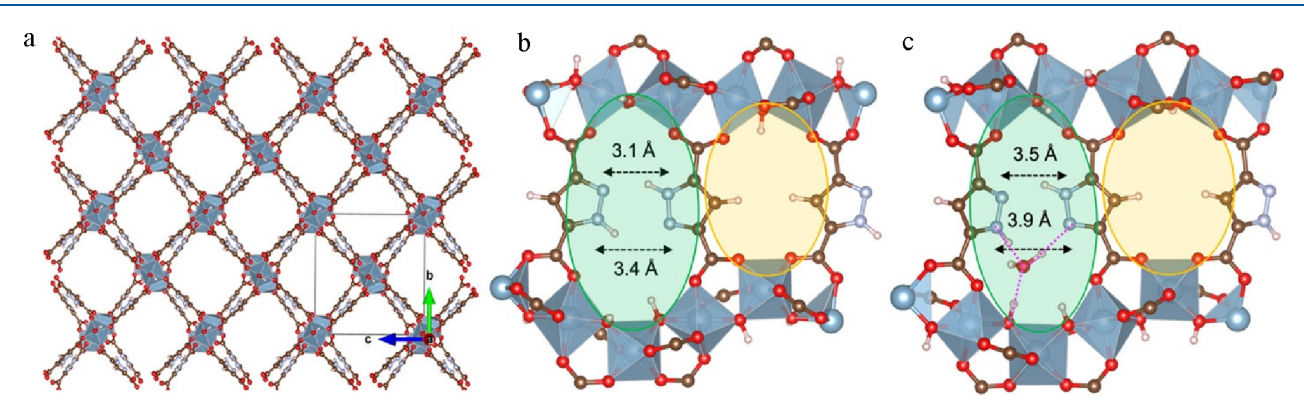


Figure 6. (a) MOF-303 is formed from infinite Al( $\mu_2$ -OH) rods aligned with the crystallographic a-axis that are connected by PZDC linkers. The image shows a 3 × 2 × 3 supercell of MOF-303 as used in the simulations. (b) Illustration of the pore walls for an asymmetric unit (for clarity, some of the surrounding atoms are shown) of the pristine MOF-303 structure. The linker arrangement with the polar parts (N-NH) of two PZDC linkers pointing toward each other and their neighboring  $\mu_2$ -OH groups leads to the formation of one strongly hydrophilic surface region (SH region shaded in green), whereas the surface region with the two CH groups of the PZDC linkers pointing toward each other is less hydrophilic (LH region shaded in yellow). The distances,  $r_{\text{NH-N}}$ , between opposite pyrazole functionalities are indicated. (c) Illustration of the primary adsorption site (located in the SH region) for water in MOF-303 through hydrogen-bond formation with neighboring N(H)<sub>linker</sub>, N<sub>linker</sub> and O<sub>rod</sub> functionalities (pink dotted lines)<sup>29</sup> Color code: Al, blue octahedra; O, red; N, light blue; C, brown; H, light pink. Reproduced with permission from Chheda et al.<sup>55</sup> 2023 American Chemical Society.

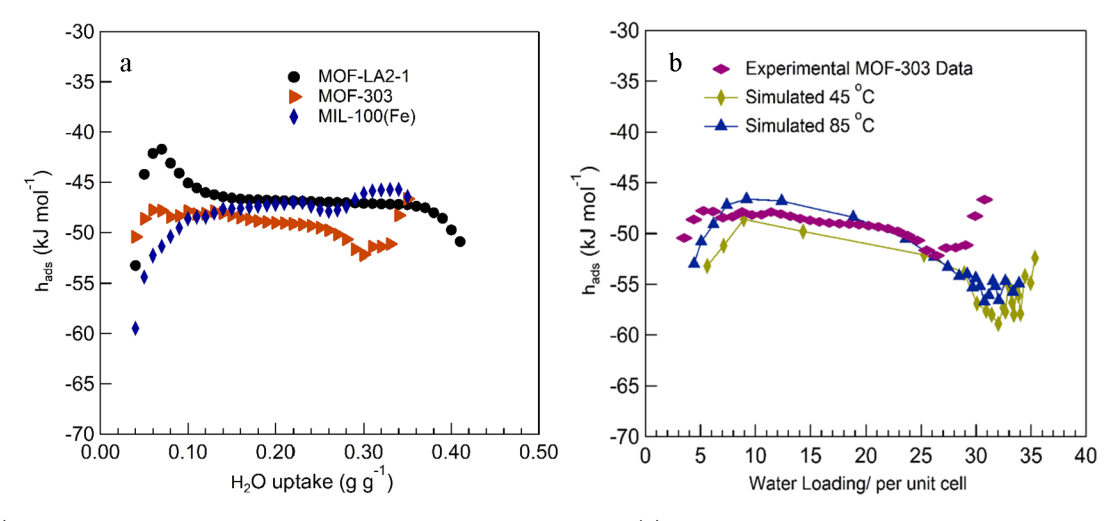
°C as compared to 25 °C. For MOF-LA2-1 additional increases in temperature result in larger decreases in capacity as compared to those of MOF-303 and provide a wider range of temperature and vacuum conditions that can be used to regenerate the MOF.

Lastly, MIL-100(Fe) was obtained from novoMOF and pure water isotherms up to 125 °C were collected (Figure 4). Unlike MOF-303 and MOF-LA2-1 which have a single step isotherm, MIL-100(Fe) has a two-step isotherm that shifts toward high RH values as the temperature increases. While less of a decrease in water adsorption capacity is observed between 25 and 45 °C the capacity did decrease, and similar to MOF-LA2-1, additional increases in temperature further decreased the capacity more so than in MOF-303.

These types of trends are consistent with those of Rudisill et al., where the shape of the isotherm and capacity of water

adsorption on activated carbon changed at elevated temperatures up to 125  $^{\circ}\text{C.}^{49}$ 

**3.3. GEMC Simulations.** To gain more insight into water adsorption behavior as well as the water adsorption sites at elevated temperatures, isobaric—isothermal Gibbs ensemble Monte Carlo (*NpT*-GEMC) simulations were performed on MOF-303. GEMC calculations were selected because the adsorption loading is an observable property in GEMC simulations that can be obtained as an ensemble average, and in *NpT*-GEMC simulations, the (gas-phase) reservoir is simulated explicitly and, hence, an equation of state is not needed. The simulated adsorption isotherms are compared to isotherms of MOF-303 collected on the volumetric apparatus, as shown in Figure 5. When the comparison is done in absolute pressure (i.e., reflecting the change in translational entropy upon adsorption), the position of the step is found to be underestimated by a consistent factor of about



pubs.acs.org/JPCC

Figure 7. (a) Experimental heat of adsorption for water on various MOFs and (b) simulated versus experimental isosteric heat of adsorption.

1.2 in the simulations compared to the experimental data (Figure 5a). As  $p_{\text{sat}}$  is approached (i.e., RH > 90%), the simulations yield a smaller decrease with increasing temperature than the experimental measurements (Figure 5b). It is known that the TIP4P model represents the energetics of water better at ambient temperature than at elevated temperatures (as evidenced by deviations in vapor-liquid coexistence curve), and this may explain why the step in the simulated isotherms is shifted to increasingly lower RH values compared to experiment (i.e., the strength of the guest-guest interactions decreases faster than the guest—host interactions). Furthermore, the simulations utilize the same rigid host structure independent of temperature, while a change in the MOF structure may also contribute to the significant decrease in the adsorption capacity from 25 to 45 °C observed in the experiments. Nevertheless, the simulated and experimental data sets do show consistent trends in the shape, and this gives confidence in the analysis of the simulation trajectories to learn about how the occupation numbers of the different known water adsorption sites change with increasing temperature.

As in prior work, 55 a set of distance-based criteria was used to identify the hydrogen-bond interactions and to calculate the number of water molecules adsorbed to the different framework adsorption sites of MOF-303. MOF-303 exhibits alternating hydrophilic and hydrophobic cavities where the hydrophilic cavities are constituted by the different H-bonding functionalities, viz. -N(H)<sub>linker</sub>, -N<sub>linker</sub>,  $\mu_2$ -(OH)<sub>rod</sub> groups. <sup>29,58</sup> Each of these hydrophilic cavities is asymmetric and consists of a wider primary patch and an opposite narrower secondary patch that adsorb water molecules through hydrogen bonds with at least one of the H-bonding functionalities of the MOF as previously detailed by Chheda et al. (Figure 6 and additional figures detailing the spatial distribution of water molecules at these sites are available in Chheda et al.). 55 The change in the occupancy of each of these water adsorption sites per unit cell at elevated temperatures was investigated at characteristic water loadings before and after the major water adsorption isotherm step.

At 2.5% RH across the temperature range (Table S2 in SI), a majority of the water molecules ( $\sim$ 4.15  $\rm H_2O$  molecules/cell at 25, 45, and 85 °C) are adsorbed in the primary patch. Adsorption at this primary patch is facilitated by about two to three hydrogen bonds. At 25 °C 96% of the water molecules in the primary patch form three H-bonds with the -N(H) $_{\rm linker}$ ,

-N<sub>linker</sub>, and  $\mu_2$ -(OH)<sub>rod</sub> groups (~3.96 H<sub>2</sub>O molecules/cell), while the number of water molecules forming the complete set of hydrogen bonds within this patch decreases slightly to 93% (3.88 H<sub>2</sub>O molecules/cell) at 85 °C due to the increased thermal motion at higher temperatures. Notably, the occupancy of the secondary patch at this RH is more than halved from ~1.75 molecules/cell to ~0.80 molecules/cell. The number of water molecules adsorbed only at the  $\mu_2$ - $(OH)_{rod}$  remains constant (0.05  $H_2O$  molecules/cell) upon increasing the temperature between 25 to 85 °C while the number of "free" water molecules (i.e., not forming a hydrogen bond) increases slightly from 0.04 to 0.06 H<sub>2</sub>O molecules/cell. Similar trends in the occupancy of the different water adsorption sites with temperature are also observed at 5.1% RH (total water uptake = 7.56 molecules/cell at 25 °C) (Table S3 in SI). The number of water molecules adsorbed in the primary patch decreases by 3%, while the number of water molecules located in the secondary patch decrease significantly by ~40% (from 2.76 to 1.58 H<sub>2</sub>O molecules/cell) upon increasing the temperature from 25 to 85 °C.

Across the temperature range, 20.5% RH corresponds to the completion of the major step in the water adsorption isotherm (Figure S19). At this higher RH, the primary patch reaches saturation. The occupancy of the strong water adsorption sites in the primary patch decreases by  $\sim$ 6% from 8.34 to 7.84  $H_2O$ molecules/cell as the temperature is increased from 25 to 85 °C. However, the number of adsorbed water molecules forming a complete set of hydrogen bonds within this primary patch remains nearly the same (~4.09 H<sub>2</sub>O molecules/cell at 25 °C and ~4.03 molecules/cell at 85 °C) while the water molecules forming an incomplete set of hydrogen bonds decreases by ~10% at the elevated temperature decrease from (~4.25 H<sub>2</sub>O molecules/cell at 25 °C to ~3.81 molecules/cell at 85 °C), which can be attributed to their lower adsorption enthalpy which is overcome by the thermal energy of the water molecules.

In contrast to the near 50% decrease found at the two lower RH values, the site occupancies of the secondary patch decrease only by ~14% at 20.5% RH (from ~7.07  $\rm H_2O$  molecules/cell at 25 °C to ~6.08  $\rm H_2O$  molecules/cell at 85 °C). The number of water molecules adsorbed at the  $\mu_2$ -(OH)<sub>rod</sub> groups (~1.65  $\rm H_2O$  molecules/cell at 25 °C) decreases to ~1.30  $\rm H_2O$  molecules/cell at 85 °C. Since this RH corresponds to the completion of the major isotherm step,

water molecules are adsorbed in the pores which form the central cavity of the 1-D channels of the MOF. At 25  $^{\circ}$ C,  $\sim$ 15.47 H<sub>2</sub>O molecules/cell ( $\sim$ 48% of the total loading) are found without a hydrogen bond to the framework. The occupancy of the central cavity decreases to  $\sim$ 10.84 H<sub>2</sub>O molecules/cell ( $\sim$ 42% of the total loading) at 85  $^{\circ}$ C.

Thus, the effect of temperature is most pronounced for water molecules adsorbed in the secondary patch at lower RH while the water uptake in the central cavity is most affected at higher RH. The occupancies of the primary patch are not largely affected across this range of RH since the primary patch constitutes the very strong water adsorption sites.

3.4. Isosteric Heats of Adsorption. The experimental heats of adsorption for MOF-303, MOF-LA2-1, and MIL-100(Fe) are shown in Figure 7 (additional data in the SI Figure S20). The first water molecules adsorb to the most active surface sites, and the heat of adsorption is larger in magnitude than that of the condensation of bulk water. These results are consistent with heats of adsorption on wood based activated carbon collected by Liu et al. 71 where the initial water bonding sites have an isosteric heat of adsorption above the heat of condensation of bulk water resulting from the hydrophilicity of the surface of the adsorbent. These results are also consistent with isosteric heat of adsorption data collected on MIL-160.<sup>72</sup> The hydrophilic nature of these initial sites is shown in Figure 7 with the heat of adsorption near 54 kJ/mol for MOF-LA2-1 and 60 kJ/mol for MIL-100(Fe), while the average isosteric heats of adsorption (Table 1) are 47 and 48 kJ/mol, respectively (details on the calculation can be found in the SI).

Table 1. Average Isosteric Heats of Adsorption Calculated from 45 to 115  $^{\circ}\mathrm{C}$ 

MOF	Average Isosteric Heat of Adsorption (kJ/mol)
novoMOF MOF-303	$50.3 \pm 1.3 \times 10^{-2}$
MOF-303	$48.9 \pm 2.1 \times 10^{-2}$
MIL-100(Fe)	$48.3 \pm 1.9 \times 10^{-2}$
Framergy MOF-303	$48.2 \pm 2.0 \times 10^{-2}$
MOF-LA2-1	$46.7 \pm 1.0 \times 10^{-2}$

The trend in the average isosteric heat of adsorption values is consistent with the decreases in capacity at temperatures above 45  $^{\circ}$ C with MOF-LA2-1 having the lowest isosteric heat of adsorption and decreasing in capacity the most at temperatures above 45  $^{\circ}$ C.

**3.5. Kinetics.** Detailed mass transfer data describing the rate of water adsorption are necessary to design, model, and optimize water harvesting systems so that simultaneous mass transfer events, such as convection and diffusion, can be quantified. To examine the rate of water adsorption, concentration swing frequency response (CSFR) was used because frequency response methods are preferred to uptake or step test methods when measuring mass transfer resistances. In particular, during uptake experiments, the gas concentration is increased in a step, the response of the adsorbent is measured (gravimetrically, volumetrically, or chromatographically), a mass transfer model is assumed, and the system response is fit to obtain a rate parameter. In many cases uptake methods fail to account for heat effects and system nonlinearities, due to

large concentration steps, are not identified or accounted for, which results in parameters with limited general significance.<sup>73</sup>

CSFR has been used previously to measure the rates of water adsorption in MOF-303, MOF-333, and 4/4-MTV-MOF<sup>40</sup> and has been described elsewhere. <sup>32,40,62,74,75</sup> In brief, the adsorption rate experiment was conducted by equilibrating each MOF with a known amount of water, after which the concentration was oscillated sinusoidally. The effluent amplitude was diminished relative to the inlet amplitude due to adsorption occurring. The ratios of the inlet and effluent amplitudes were calculated, and data points for each oscillation frequency are shown in Figure 8a and Figure 8b.

The data in Figure 8 were fit to both a linear driving force model and a micropore diffusion model. The linear driving force model can be used for describing systems in which the rate-limiting mass transfer step is a surface barrier where a constriction at the pore mouth is the dominant resistance, and the micropore diffusion model is the governing rate-limiting mechanism based on a description of the microparticle as spherical in the nanoporous domain. Ta,76 For both MOF-LA2-1 and MIL-100(Fe) water adsorption is rate-limited by micropore diffusion through the pore, which is consistent with water diffusion rates in other MOFs.

Next, the Darken relation was used to predict the rate of micropore diffusion as a function of isotherm loading based on the data collected at 40% RH and 50% RH of MOF-LA2-1 and MIL-100(Fe) respectively (Figure 8c,d and Table 2). Based on the limited adsorption hysteresis reported in these samples previously, it was assumed that the adsorption and desorption isotherm slopes were the same and the adsorption isotherm slope was used to complete the calculation. 25,35,36 The Darkenpredicted diffusion rate data show the expected dependence on loading, where diffusion slows at the step in the isotherm corresponding with all the strong adsorption sites being occupied. The large change in the isotherm slope arises from increased guest-guest interactions (adsorbate-adsorbate), which has an impact on the transport diffusion rate. This has been detailed previously for S-shaped isotherms and has been shown to result in adsorption where the self-diffusion (or tracer diffusion of tagged particles) is greater than the transport diffusion." This is consistent with previously reported MOF-303 diffusion data reported by Lassitter et al. where the diffusion rate was determined at various loadings across the isotherm.40

#### 4. CONCLUSION

Elevated temperature water isotherms on MOF-LA2-1, MOF-303, and MIL-100(Fe) provide detailed thermodynamic conditions where heat and vacuum can be used to regenerate these materials and provide a method to examine the maximum possible working capacity that can be achieved under specific regeneration conditions. Molecular simulations show that as the temperature of the adsorption is increased, the water adsorption in the strongest adsorption sites, the primary patch, does not change appreciably. At lower RH and higher temperature, the secondary adsorption patch sees a reduction in loading, and at higher RH a reduction in loading is observed in the broader pore space. With a wide range of isotherms from 45 to 125 °C the calculated heats of adsorption as a function of loading are consistent with previous reports for these MOFs and show active initial adsorption sites with heats of adsorption higher than those of the condensation of bulk water. The diffusion rate of water through these materials can be described

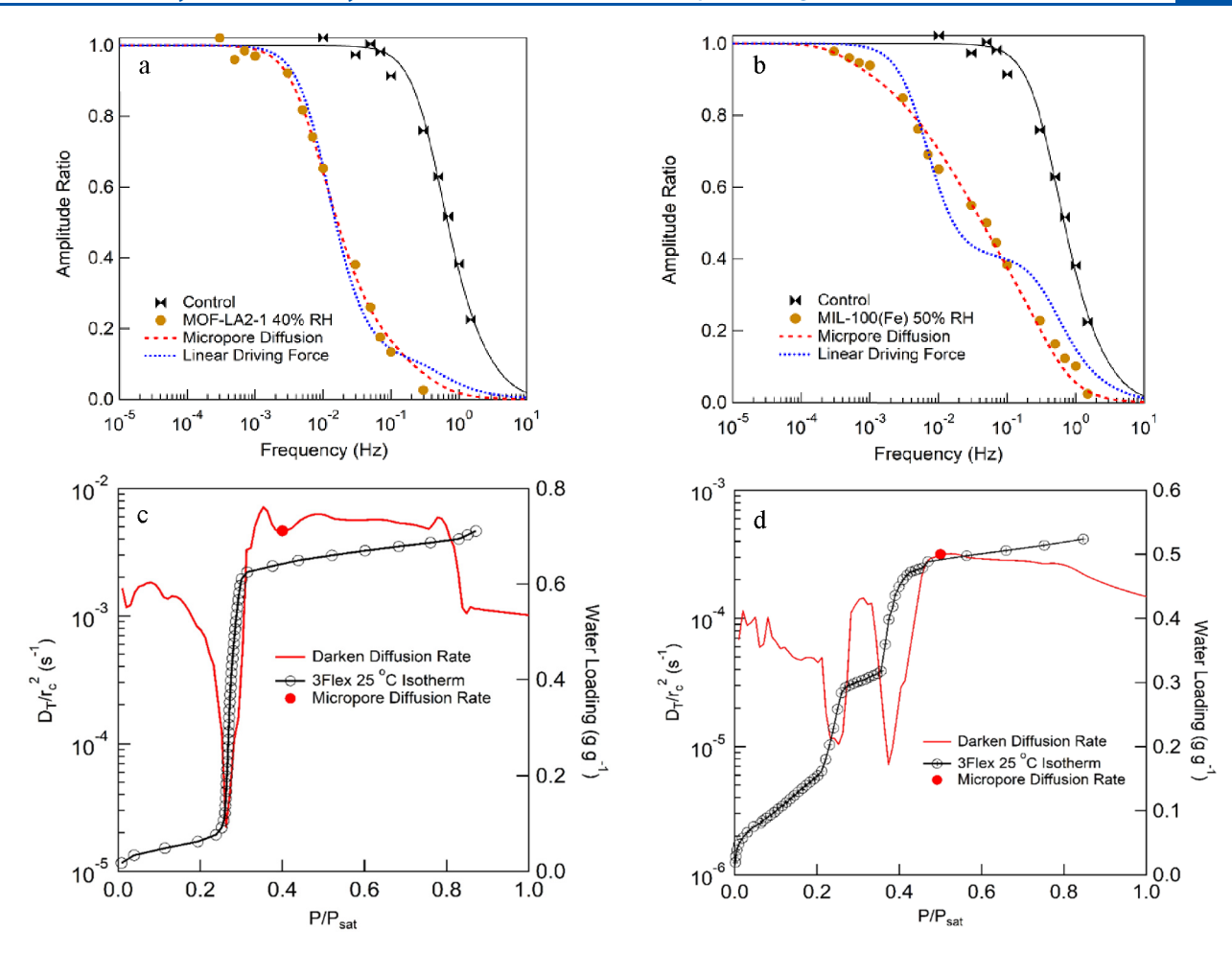


Figure 8. (a) Frequency response curves for MOF-LA2-1 and (b) MIL-100(Fe) and the Darken rate of micropore diffusion plotted alongside the water adsorption isotherm for (c) MOF-LA2-1 and (d) MIL-100(Fe).

Table 2. Water Diffusion Rates for MOF-LA2-1 and MIL-100(Fe)

MOF	Diffusion Rate (s-1)
MOF-LA2-1	4.65 x 10 <sup>-3</sup>
MIL-100(Fe)	3.17 x 10 <sup>-4</sup>

with a micropore diffusion model, and the Darken relationship shows significant reductions in the perceived adsorption rate due to the thermodynamic effects of the isotherms slope. More broadly, the data show precise control over high-temperature isotherm shape that can be provided by reticular chemistry and provide key insight into the application of these materials in water capture systems.

#### ASSOCIATED CONTENT

## **5** Supporting Information

The Supporting Information is available free of charge at https://pubs.acs.org/doi/10.1021/acs.jpcc.4c01733.

Breakthrough apparatus and volumetric apparatus design, isosteric heat of adsorption data and calculation methodology, simulation details and simulation methodology for calculating isosteric heats of adsorption, CSFR apparatus details and Darken methodology for extrapolating diffusion rates, pure component isotherms, nitrogen isotherms at 77 K, PXRD patterns, water

isotherm comparisons from 25 to 125 °C, Lennard-Jones parameters and partial charges (PDF)

#### AUTHOR INFORMATION

### **Corresponding Author**

T. Grant Glover — Department of Chemical and Biomolecular Engineering, University of South Alabama, Mobile, Alabama 36688, United States; orcid.org/0000-0002-3393-6038; Email: glover@southalabama.edu

#### **Authors**

Jon Hastings — Department of Chemical and Biomolecular Engineering, University of South Alabama, Mobile, Alabama 36688, United States; Orcid.org/0009-0002-6222-5988

Thomas Lassitter – Department of Chemical and Biomolecular Engineering, University of South Alabama, Mobile, Alabama 36688, United States

Zhiling Zheng — Department of Chemistry, University of California, Berkeley, California 94720, United States;
occid.org/0000-0001-6090-2258

Saumil Chheda — Department of Chemical Engineering and Materials Science, Department of Chemistry and Chemical Theory Center, University of Minnesota—Twin Cities, Minneapolis, Minnesota 55455, United States; ○ orcid.org/0000-0002-0989-5707

J. Ilja Siepmann – Department of Chemical Engineering and Materials Science, Department of Chemistry and Chemical Theory Center, University of Minnesota—Twin Cities, Minneapolis, Minnesota 55455, United States; orcid.org/0000-0003-2534-4507

Laura Gagliardi — Department of Chemistry, Pritzker School of Molecular Engineering, and Chicago Center for Theoretical Chemistry, University of Chicago, Chicago, Illinois 60637, United States; orcid.org/0000-0001-5227-1396

Omar M. Yaghi — Department of Chemistry, University of California, Berkeley, California 94720, United States;
o orcid.org/0000-0002-5611-3325

Complete contact information is available at: https://pubs.acs.org/10.1021/acs.jpcc.4c01733

#### **Notes**

The authors declare the following competing financial interest(s): O.M.Y. is a co-founder of Water Harvesting Inc. and ATOCO Inc., aiming at commercializing related technologies. T.G.G. is a co-founder of ATOCO Inc. The remaining authors declare no competing interests.

## ACKNOWLEDGMENTS

This material is based on work supported by the Defense Advanced Research Projects Agency (DARPA) under contract HR001-21-C0020 and the Department of Energy, Office of Basic Energy Sciences, Division of Chemical Sciences, Geosciences and Biosciences under Awards DE-FG02-17ER16362 and DE-SC0023454 (S.C. and J.I.S.), and the National Science Foundation, Division of Chemistry, Chemical Structure, Dynamics, and Mechanisms A (CSDM-A) Award Number: CHE-2223442 (L.G. and O.M.Y.). Any opinions, findings, conclusions, or recommendations expressed in this material are those of the author(s) and do not necessarily reflect the views of DARPA. J.H. acknowledges financial support from the Alabama Graduate Research Scholars Program (GRSP) funded through the Alabama Commission for Higher Education and administered by the Alabama EPSCoR. The authors thank The Minnesota Supercomputing Institute for providing the computational resources used for simulating the water adsorption isotherms presented in this work. This research was supported in part by the NASA ESPSCOR AL-19-EPSCoR-0002.

# REFERENCES

- (1) Nandakumar, D. K.; Zhang, Y.; Ravi, S. K.; Guo, N.; Zhang, C.; Tan, S. C. Solar Energy Triggered Clean Water Harvesting from Humid Air Existing above Sea Surface Enabled by a Hydrogel with Ultrahigh Hygroscopicity. *Adv. Mater.* **2019**, *31* (10), No. 1806730.
- (2) Zhou, X.; Lu, H.; Zhao, F.; Yu, G. Atmospheric Water Harvesting: A Review of Material and Structural Designs. ACS Mater. Lett. 2020, 2 (7), 671–684.
- (3) Lord, J.; Thomas, A.; Treat, N.; Forkin, M.; Bain, R.; Dulac, P.; Behroozi, C. H.; Mamutov, T.; Fongheiser, J.; Kobilansky, N.; et al. Global Potential for Harvesting Drinking Water from Air Using Solar Energy. *Nature* **2021**, *598* (7882), *611–617*.
- (4) Wang, M.; Liu, E.; Jin, T.; Zafar, S.; Mei, X.; Fauconnier, M.-L.; De Clerck, C. Towards a Better Understanding of Atmospheric Water Harvesting (AWH) Technology. *Water Res.* **2024**, 250, No. 121052.
- (5) Jarimi, H.; Powell, R.; Riffat, S. Review of Sustainable Methods for Atmospheric Water Harvesting. *Int. J. Low-Carbon Technol.* **2020**, 15 (2), 253–276.
- (6) Anjali, C.; Renuka, N. K. Atmospheric Water Harvesting: Prospectus on Graphene-Based Materials. *J. Mater. Res.* **2022**, 37 (14), 2227–2240.

- (7) Rieth, A. J.; Yang, S.; Wang, E. N.; Dincă, M. Record Atmospheric Fresh Water Capture and Heat Transfer with a Material Operating at the Water Uptake Reversibility Limit. *ACS Cent. Sci.* **2017**, 3 (6), 668–672.
- (8) Oki, T.; Kanae, S. Global Hydrological Cycles and World Water Resources. *Science* **2006**, 313 (5790), 1068–1072.
- (9) Zhang, S.; Fu, J.; Xing, G.; Zhu, W.; Ben, T. Porous Materials for Atmospheric Water Harvesting. *ChemistryOpen* **2023**, *12* (5), No. e202300046.
- (10) Liu, X.; Beysens, D.; Bourouina, T. Water Harvesting from Air: Current Passive Approaches and Outlook. ACS Mater. Lett. 2022, 4 (5), 1003–1024.
- (11) Wang, J.; Hua, L.; Li, C.; Wang, R. Atmospheric Water Harvesting: Critical Metrics and Challenges. *Energy Environ. Sci.* **2022**, 15 (12), 4867–4871.
- (12) Wasti, T. Z.; Sultan, M.; Aleem, M.; Sajjad, U.; Farooq, M.; Raza, H. M.; Khan, M. U.; Noor, S. An Overview of Solid and Liquid Materials for Adsorption-Based Atmospheric Water Harvesting. *Adv. Mech. Eng.* **2022**, *14* (3), No. 168781322210827.
- (13) Tashtoush, B.; Alshoubaki, A. Atmospheric Water Harvesting: A Review of Techniques, Performance, Renewable Energy Solutions, and Feasibility. *Energy* **2023**, *280*, No. 128186.
- (14) Tu, Y.; Wang, R.; Zhang, Y.; Wang, J. Progress and Expectation of Atmospheric Water Harvesting. *Joule* **2018**, 2 (8), 1452–1475.
- (15) Yang, K.; Pan, T.; Lei, Q.; Dong, X.; Cheng, Q.; Han, Y. A Roadmap to Sorption-Based Atmospheric Water Harvesting: From Molecular Sorption Mechanism to Sorbent Design and System Optimization. *Environ. Sci. Technol.* **2021**, *55* (10), 6542–6560.
- (16) Eisenstein, M. Fresh Water from Thin Air. Nature 2023.
- (17) Meng, Y.; Dang, Y.; Suib, S. L. Materials and Devices for Atmospheric Water Harvesting. *Cell Rep. Phys. Sci.* **2022**, 3 (7), No. 100976.
- (18) Ejeian, M.; Wang, R. Z. Adsorption-Based Atmospheric Water Harvesting. *Joule* **2021**, *5* (7), 1678–1703.
- (19) LaPotin, A.; Kim, H.; Rao, S. R.; Wang, E. N. Adsorption-Based Atmospheric Water Harvesting: Impact of Material and Component Properties on System-Level Performance. *Acc. Chem. Res.* **2019**, *52* (6), 1588–1597.
- (20) Kim, H.; Rao, S. R.; Kapustin, E. A.; Zhao, L.; Yang, S.; Yaghi, O. M.; Wang, E. N. Adsorption-Based Atmospheric Water Harvesting Device for Arid Climates. *Nat. Commun.* **2018**, *9* (1), 1191.
- (21) Bilal, M.; Sultan, M.; Morosuk, T.; Den, W.; Sajjad, U.; Aslam, M. M. A.; Shahzad, M. W.; Farooq, M. Adsorption-Based Atmospheric Water Harvesting: A Review of Adsorbents and Systems. *Int. Commun. Heat Mass Transfer* **2022**, *133*, No. 105961.
- (22) Aghajani Hashjin, M.; Zarshad, S.; Motejadded Emrooz, H. B.; Sadeghzadeh, S. Enhanced Atmospheric Water Harvesting Efficiency through Green-Synthesized MOF-801: A Comparative Study with Solvothermal Synthesis. *Sci. Rep.* **2023**, *13* (1), 16983.
- (23) Zhang, W.; Xia, Y.; Wen, Z.; Han, W.; Wang, S.; Cao, Y.; He, R.-X.; Liu, Y.; Chen, B. Enhanced Adsorption-Based Atmospheric Water Harvesting Using a Photothermal Cotton Rod for Freshwater Production in Cold Climates. *RSC Adv.* **2021**, *11* (56), 35695–35702.
- (24) Kim, H.; Rao, S. R.; LaPotin, A.; Lee, S.; Wang, E. N. Thermodynamic Analysis and Optimization of Adsorption-Based Atmospheric Water Harvesting. *Int. J. Heat Mass Transfer* **2020**, *161*, No. 120253.
- (25) Bilal, M.; Sultan, M.; Majeed, F.; Farooq, M.; Sajjad, U.; Ibrahim, S. M.; Khan, M. U.; Azizi, S.; Javaid, M. Y.; Ahmad, R. Investigating Adsorption-Based Atmospheric Water Harvesting Potential for Pakistan. *Sustainability* **2022**, *14* (19), 12582.
- (26) Deng, F.; Chen, Z.; Wang, C.; Xiang, C.; Poredoš, P.; Wang, R. Hygroscopic Porous Polymer for Sorption-Based Atmospheric Water Harvesting. *Adv. Sci.* **2022**, *9* (33), No. 2204724.
- (27) LaPotin, A.; Zhong, Y.; Zhang, L.; Zhao, L.; Leroy, A.; Kim, H.; Rao, S. R.; Wang, E. N. Dual-Stage Atmospheric Water Harvesting Device for Scalable Solar-Driven Water Production. *Joule* **2021**, *5* (1), 166–182.

- (28) Chen, Z.; Song, S.; Ma, B.; Li, Y.; Shao, Y.; Shi, J.; Liu, M.; Jin, H.; Jing, D. Recent Progress on Sorption/Desorption-Based Atmospheric Water Harvesting Powered by Solar Energy. *Sol. Energy Mater. Sol. Cells* **2021**, 230, No. 111233.
- (29) Hanikel, N.; Pei, X.; Chheda, S.; Lyu, H.; Jeong, W.; Sauer, J.; Gagliardi, L.; Yaghi, O. M. Evolution of Water Structures in Metal-Organic Frameworks for Improved Atmospheric Water Harvesting. *Science* **2021**, *374* (6566), 454–459.
- (30) Yaghi, O. M. Reticular Chemistry—Construction, Properties, and Precision Reactions of Frameworks. *J. Am. Chem. Soc.* **2016**, 138 (48), 15507–15509.
- (31) Jiao, L.; Seow, J. Y. R.; Skinner, W. S.; Wang, Z. U.; Jiang, H.-L. Metal—Organic Frameworks: Structures and Functional Applications. *Mater. Today* **2019**, *27*, 43–68.
- (32) Gas Adsorption in Metal-Organic Frameworks: Fundamentals and Applications; Glover, T. G., Mu, B., Eds.; CRC Press: Boca Raton, FL, 2018
- (33) Yaghi, O. M.; Kalmutzki, M. J.; Diercks, C. S. Introduction to Reticular Chemistry: Metal-Organic Frameworks and Covalent Organic Frameworks; Wiley: 2019.
- (34) Shi, W.; Guan, W.; Lei, C.; Yu, G. Sorbents for Atmospheric Water Harvesting: From Design Principles to Applications. *Angew. Chem., Int. Ed.* **2022**, *61* (43), No. e202211267.
- (35) Hanikel, N.; Kurandina, D.; Chheda, S.; Zheng, Z.; Rong, Z.; Neumann, S. E.; Sauer, J.; Siepmann, J. I.; Gagliardi, L.; Yaghi, O. M. MOF Linker Extension Strategy for Enhanced Atmospheric Water Harvesting. ACS Cent. Sci. 2023, 9 (3), 551–557.
- (36) Feng, X.; Qin, M.; Cui, S.; Rode, C. Metal-Organic Framework MIL-100(Fe) as a Novel Moisture Buffer Material for Energy-Efficient Indoor Humidity Control. *Build. Environ.* **2018**, *145*, 234–242.
- (37) Ahrestani, Z.; Sadeghzadeh, S.; Emrooz, H. B. M. An Overview of Atmospheric Water Harvesting Methods, the Inevitable Path of the Future in Water Supply. *RSC Adv.* **2023**, *13* (15), 10273–10307.
- (38) Gao, J.; Fei, S.; Ho, Y.-L.; Matsuda, R.; Daiguji, H.; Delaunay, J.-J. Water Confined in MIL-101(Cr): Unique Sorption—Desorption Behaviors Revealed by Diffuse Reflectance Infrared Spectroscopy and Molecular Dynamics Simulation. *J. Phys. Chem. C* **2021**, *125* (32), 17786—17795.
- (39) Zheng, Z.; Alawadhi, A. H.; Yaghi, O. M. Green Synthesis and Scale-Up of MOFs for Water Harvesting from Air. *Mol. Front. J.* **2023**, 1–20.
- (40) Lassitter, T.; Hanikel, N.; Coyle, D. J.; Hossain, M. I.; Lipinski, B.; O'Brien, M.; Hall, D. B.; Hastings, J.; Borja, J.; O'Neil, T.; Ephraim Neumann, S.; Moore, D. R.; Yaghi, O. M.; Grant Glover, T. Mass Transfer in Atmospheric Water Harvesting Systems. *Chem. Eng. Sci.* 2024, 285, No. 119430.
- (41) Hanikel, N.; Prévot, M. S.; Fathieh, F.; Kapustin, E. A.; Lyu, H.; Wang, H.; Diercks, N. J.; Glover, T. G.; Yaghi, O. M. Rapid Cycling and Exceptional Yield in a Metal-Organic Framework Water Harvester. ACS Cent. Sci. 2019, 5 (10), 1699–1706.
- (42) Al Mesfer, M. K.; Danish, M. Breakthrough Adsorption Study of Activated Carbons for CO2 Separation from Flue Gas. *J. Environ. Chem. Eng.* **2018**, *6* (4), 4514–4524.
- (43) Wilkins, N. S.; Rajendran, A.; Farooq, S. Dynamic Column Breakthrough Experiments for Measurement of Adsorption Equilibrium and Kinetics. *Adsorption* **2021**, *27* (3), 397–422.
- (44) Silva, M. P.; Ribeiro, A. M.; Silva, C. G.; Nogueira, I. B. R.; Cho, K.-H.; Lee, U.-H.; Faria, J. L.; Loureiro, J. L.; Chang, J.-S.; Rodrigues, A. E.; et al. MIL-160(Al) MOF's Potential in Adsorptive Water Harvesting. *Adsorption* **2021**, 27 (2), 213–226.
- (45) Lyu, H.; Chen, O. I.-F.; Hanikel, N.; Hossain, M. I.; Flaig, R. W.; Pei, X.; Amin, A.; Doherty, M. D.; Impastato, R. K.; Glover, T. G.; Moore, D. R.; Yaghi, O. M. Carbon Dioxide Capture Chemistry of Amino Acid Functionalized Metal—Organic Frameworks in Humid Flue Gas. J. Am. Chem. Soc. 2022, 144 (5), 2387—2396.
- (46) Rajendran, A.; Shimizu, G. K. H.; Woo, T. K. The Challenge of Water Competition in Physical Adsorption of CO2 by Porous Solids

- for Carbon Capture Applications A Short Perspective. *Adv. Mater.* **2024**, *36* (12), No. 2301730.
- (47) Bozbiyik, B.; Van Assche, T.; Lannoeye, J.; De Vos, D. E.; Baron, G. V.; Denayer, J. F. M. Stepped Water Isotherm and Breakthrough Curves on Aluminium Fumarate Metal—Organic Framework: Experimental and Modelling Study. *Adsorption* **2017**, 23 (1), 185–192.
- (48) Grant Glover, T.; Peterson, G. W.; Schindler, B. J.; Britt, D.; Yaghi, O. MOF-74 Building Unit Has a Direct Impact on Toxic Gas Adsorption. *Chem. Eng. Sci.* **2011**, *66* (2), 163–170.
- (49) Rudisill, E. N.; Hacskaylo, J. J.; LeVan, M. D. Coadsorption of Hydrocarbons and Water on BPL Activated Carbon. *Ind. Eng. Chem. Res.* 1992, 31 (4), 1122–1130.
- (50) Sircar, S.; Mohr, R.; Ristic, C.; Rao, M. B. Isosteric Heat of Adsorption: Theory and Experiment. *J. Phys. Chem. B* **1999**, *103* (31), 6539–6546.
- (51) Pan, H.; Ritter, J. A.; Balbuena, P. B. Examination of the Approximations Used in Determining the Isosteric Heat of Adsorption from the Clausius—Clapeyron Equation. *Langmuir* 1998, 14 (21), 6323—6327.
- (52) Panagiotopoulos, A. Z. Direct Determination of Phase Coexistence Properties of Fluids by Monte Carlo Simulation in a New Ensemble. *Mol. Phys.* **1987**, *61* (4), 813–826.
- (53) Panagiotopoulos, A. Z.; Quirke, N.; Stapleton, M.; Tildesley, D. J. Phase Equilibria by Simulation in the Gibbs Ensemble. *Mol. Phys.* **1988**, *63* (4), 527–545.
- (54) Siepmann, J. I.; Martin, M. G.; Chen, B.; Wick, C.; Stubbs, J. M.; Potoff, J. J.; Eggimann, B. L.; McGrath, M. J.; Zhao, X. S.; Anderson, K. E.; et al. *Monte Carlo for Complex Chemical Systems—Minnesota, Version* 20.2; University of Minnesota: Minneapolis, MN, 2020
- (55) Chheda, S.; Jeong, W.; Hanikel, N.; Gagliardi, L.; Siepmann, J. I. Monte Carlo Simulations of Water Adsorption in Aluminum Oxide Rod-Based Metal—Organic Frameworks. *J. Phys. Chem. C* **2023**, *127* (16), 7837—7851.
- (56) Grimme, S.; Ehrlich, S.; Goerigk, L. Effect of the Damping Function in Dispersion Corrected Density Functional Theory. *J. Comput. Chem.* **2011**, 32 (7), 1456–1465.
- (57) Kresse, G.; Furthmüller, J. Efficiency of Ab-Initio Total Energy Calculations for Metals and Semiconductors Using a Plane-Wave Basis Set. *Comput. Mater. Sci.* **1996**, *6* (1), 15–50.
- (58) Jorgensen, W. L.; Chandrasekhar, J.; Madura, J. D.; Impey, R. W.; Klein, M. L. Comparison of Simple Potential Functions for Simulating Liquid Water. *J. Chem. Phys.* **1983**, 79 (2), 926–935.
- (59) Vega, C.; Abascal, J. L. F.; Nezbeda, I. Vapor-Liquid Equilibria from the Triple Point up to the Critical Point for the New Generation of TIP4P-like Models: TIP4P/Ew, TIP4P/2005, and TIP4P/Ice. *J. Chem. Phys.* **2006**, *125* (3), No. 034503.
- (60) Chen, J. L.; Xue, B.; Mahesh, K.; Siepmann, J. I. Molecular Simulations Probing the Thermophysical Properties of Homogeneously Stretched and Bubbly Water Systems. *J. Chem. Eng. Data* **2019**, *64* (9), 3755–3771.
- (61) Xue, B.; Harwood, D. B.; Chen, J. L.; Siepmann, J. I. Monte Carlo Simulations of Fluid Phase Equilibria and Interfacial Properties for Water/Alkane Mixtures: An Assessment of Nonpolarizable Water Models and of Departures from the Lorentz–Berthelot Combining Rules. J. Chem. Eng. Data 2018, 63 (11), 4256–4268.
- (62) Glover, T. G.; Wang, Y.; LeVan, M. D. Diffusion of Condensable Vapors in Single Adsorbent Particles Measured via Concentration-Swing Frequency Response. *Langmuir* **2008**, *24* (23), 13406–13413.
- (63) Ruthven, D. M. Principles of Adsorption and Adsorption Processes; John Wiley & Sons: 1984.
- (64) Ruthven, D. M.; Brandani, S.; Eic, M. Measurement of Diffusion in Microporous Solids by Macroscopic Methods. *Mol. Sieves Sci. Technol.* **2008**, *7* (December2005), 45–84.
- (65) Ruthven, D. M. Sorption Kinetics for Diffusion-Controlled Systems with a Strongly Concentration-Dependent Diffusivity. *Chem. Eng. Sci.* **2004**, 59 (21), 4531–4545.

- (66) Kärger, J.; Ruthven, D. M. Diffusion in Nanoporous Materials: Fundamental Principles, Insights and Challenges. *New J. Chem.* **2016**, 40 (5), 4027–4048.
- (67) Wolff, L.; Jamali, S. H.; Becker, T. M.; Moultos, O. A.; Vlugt, T. J. H.; Bardow, A. Prediction of Composition-Dependent Self-Diffusion Coefficients in Binary Liquid Mixtures: The Missing Link for Darken-Based Models. *Ind. Eng. Chem. Res.* **2018**, *57* (43), 14784–14794.
- (68) Rutherford, S. W.; Coons, J. E. Adsorption Dynamics of Carbon Dioxide in Molecular Sieving Carbon. *Carbon* **2003**, *41* (3), 405–411
- (69) Rutherford, S. W.; Do, D. D. Adsorption Dynamics Measured by Permeation and Batch Adsorption Methods. *Chem. Eng. J.* **2000**, *76* (1), 23–31.
- (70) Darken, L. S. Diffusion, Mobility and Their Interrelation through Free Energy in Binary Metallic System. *Trans. AIME* **1948**, 175, 184–201.
- (71) Liu, L.; Tan, S.; Horikawa, T.; Do, D. D.; Nicholson, D.; Liu, J. Water Adsorption on Carbon A Review. *Adv. Colloid Interface Sci.* **2017**, 250, 64–78.
- (72) Solovyeva, M.; Krivosheeva, I.; Gordeeva, L.; Aristov, Y. MIL-160 as an Adsorbent for Atmospheric Water Harvesting. *Energies* **2021**, *14* (12), 3586.
- (73) Wang, Y.; LeVan, M. D. Master Curves for Mass Transfer in Bidisperse Adsorbents for Pressure-Swing and Volume-Swing Frequency Response Methods. *AIChE J.* **2011**, *57* (8), 2054–2069.
- (74) Wang, Y.; Mahle, J. J.; Furtado, A. M. B.; Glover, T. G.; Buchanan, J. H.; Peterson, G. W.; LeVan, M. D. Mass Transfer and Adsorption Equilibrium for Low Volatility Alkanes in BPL Activated Carbon. *Langmuir* **2013**, *29* (9), 2935–2945.
- (75) Hossain, M. I.; Glover, T. G. Kinetics of Water Adsorption in UiO-66 MOF. *Ind. Eng. Chem. Res.* **2019**, 58 (24), 10550–10558.
- (76) Tovar, T. M.; Zhao, J.; Nunn, W. T.; Barton, H. F.; Peterson, G. W.; Parsons, G. N.; LeVan, M. D. Diffusion of CO2 in Large Crystals of Cu-BTC MOF. *J. Am. Chem. Soc.* **2016**, *138* (36), 11449–11452.
- (77) Chmelik, C.; Bux, H.; Caro, J.; Heinke, L.; Hibbe, F.; Titze, T.; Kärger, J. Mass Transfer in a Nanoscale Material Enhanced by an Opposing Flux. *Phys. Rev. Lett.* **2010**, *104* (8), No. 085902.